RESEARCH ARTICLE

Advancing Baud Rate Receivers: On Multiple CTLE Parameters Background Adaptation

YANG AZEVEDO TAVARES, (Student Member, IEEE),
AND MINJAE LEE, (Senior Member, IEEE)

School of Electrical Engineering and Computer Science, Gwangju Institute of Science and Technology, Buk-gu, Gwangju 61005, South Korea

Corresponding author: Minjae Lee (minjae@gist.ac.kr)

ABSTRACT The continuous-time linear equalizer (CTLE) is a key component in receivers for improving the achievable bit error rate. Available CTLE background adaptation methods are limited to adjusting a single parameter, such as the source resistance or capacitance. In contrast, this paper presents a background adaptation method capable of concurrently finding near-optimal source resistance and capacitance values for multiple CTLE configurations in baud rate communication. Moreover, this paper presents a sequential method for adjusting both short and long-tail CTLE parameters, ensuring effective system control. The multiple loop interactions are considered with recent DSP-based receivers main building blocks, such as the clock and data recovery (CDR) and automatic gain control (AGC). A relatively simple logic based on inter-symbol interference (ISI) taps is employed, similar to conventional Mueller-Muller methods, which does not impose significant hardware overhead compared to previous publications. Simulations using real channel models demonstrate the proposed adaptation's performance across a wide range of insertion loss channels and various modulations.

INDEX TERMS Adaptation, equalization, linear equalizer, receiver, digital signal processing.

I. INTRODUCTION

Data-intensive applications are becoming more prevalent with the continuous advancement of state-of-the-art technologies, such as artificial intelligence, big data analytics and cloud computing. A 224Gb/s per-lane transceiver has already been published [1], [2], and the per-lane data rate trend indicates a doubling every 3-4 years in wireline applications [1]. In contrast, communication interfaces must support legacy channels to avoid expensive infrastructure upgrades, which may suffer from significant insertion loss (IL) and cross-talk interference [3].

Fig. 1(a) shows the channel response along with the near-end crosstalk (NEXT) and far-end crosstalk (FEXT) of a backplane channel [4] where, at 40 GHz, NEXT crosstalk surpasses the through port, causing unreliable communication. Increasing pulse-amplitude modulation (PAM) orders can reduce the required bandwidth for the same data rates,

avoiding low signal-to-noise ratio (SNR) frequency regions. For instance, by looking into Fig. 1(a), it could be better to have a PAM-4 signal with 25 GHz bandwidth rather than a PAM-2 signal with 50 GHz bandwidth to avoid the negative SNR region. However, higher PAM orders also elevate the inter-symbol interference (ISI) correction requirements. The analog-to-digital converter based on a digital signal processor (ADC-DSP-based) receivers have been preferred for high-loss, high-data-rate setups due to their flexibility, technology scaling, and robustness against process, voltage, and temperature variations (PVT) [1], [3], [5], [6], [7]. Nevertheless, an analog receiver has been published for a comparable target [8]. Fig. 1(b) depicts a block diagram of a typical ADC-DSP-based receiver for baud rate systems, incorporating clock-to-data recovery (CDR), continuous-time linear equalizer (CTLE), automatic gain control (AGC), feed-forward equalizer (FFE), and decision feedback equalizer (DFE) adaptation loops. Moreover, the employment of an additional CTLE for long-tail ISI (also denoted as mid-CTLE in this paper) is becoming popular [6],

---

The associate editor coordinating the review of this manuscript and approving it for publication was Tianhua Xu.
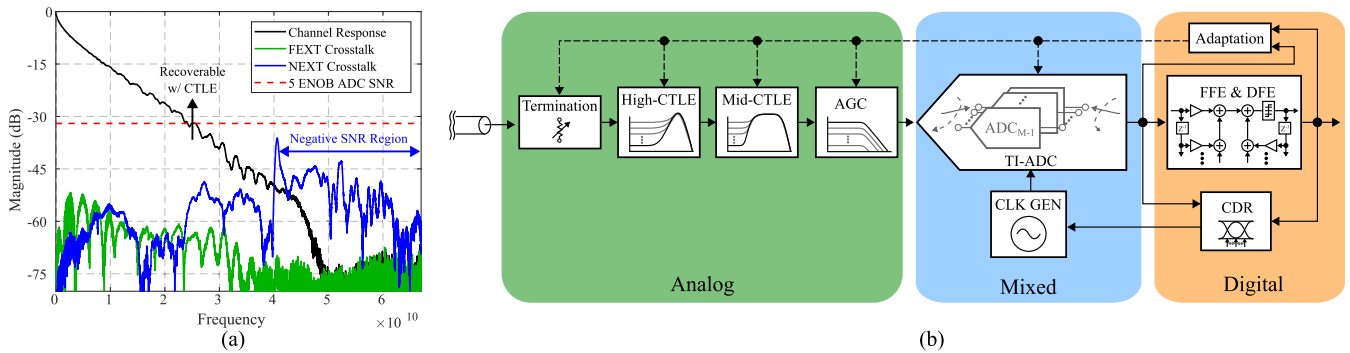
FIGURE 1. (a) Frequency response of a backplane channel [9] through port, far-end crosstalk (FEXT) and near-end crosstalk (NEXT). The standard required ADC SNR for a PAM-4 receiver is also highlighted along with the negative SNR region and the CTLE equalization task to recover the input high-frequency magnitude before the ADC noise is added. (b) The main building blocks of an ADC-DSP-based receiver. A channel delivers a signal to the receiver termination, high-CTLE, mid-CTLE and AGC in the analog domain and the TI-ADC samples it in the mixed domain. In this paper, the short and long-tail CTLEs are denoted as high-CTLE and mid-CTLE, respectively. Furthermore, the signal is digitally processed by the FFE, DFE and CDR in the digital domain. The processed samples are used for the adaptation of all the main building blocks in the receiver.

[14], [15]. The standard CTLE with frequency peaking at the Nyquist frequency (half of the sampling frequency) is denoted as high-CTLE in this paper. The mixed-style scheme in Fig. 1(b) employs equalization in both analog and digital domains. Fig. 1(a) also shows the SNR line for a 5 effective number of bits (ENOB) ADC, the standard resolution for recent ADC-DSP-based PAM-4 receivers [16], [17]. The CTLE mitigates ISI, reducing the impact of ADC quantization and thermal noise boosted by the FFE. Designing a high ENOB ADC at very high frequencies is challenging due to jitter and linearity limitations [17], [18], [19]. Additionally, the CTLE plays a crucial role in optimizing the CDR by improving the gain-to-noise ratio (KNR) and jitter tolerance (JTOL) [20].

There are a few published methods for the CTLE adaptation. Fig. 2 illustrates good representatives of available CTLE techniques [10], [11], [12], [13], [21]. In [10], a CTLE adaptation method is presented where low-pass and high-pass filters compare the low and high-frequency magnitudes of the input signal to detect the equalization amount as shown in Fig. 2(a). However, the implementation of filters adds parasitics at the input path which may limit the achievable bandwidth. In [21], a similar concept is presented. Moreover, the comparison of low and high-frequency magnitudes supplies only one degree of freedom for adaptation control. In [11], a CTLE adaptation method is presented where the eye transition statistics are measured to estimate the equalization amount. The optimum code is considered to be found when the transition samples standard deviation is minimized as shown in Fig. 2(b). The main drawback lies in the need for over-sampling (not baud rate) to extract the eye transition statistics. Likewise, the single error information limits the calibration degree of freedom as it only tunes the source resistance. In [12], a sign-sign least-mean-squares (SSLMS) is employed to minimize the sum of the post-taps f_4 and f_5 as shown in Fig. 2(c). The considered taps for minimization are based on the DFE correction capability over the channel characteristics and this adaptation only controls
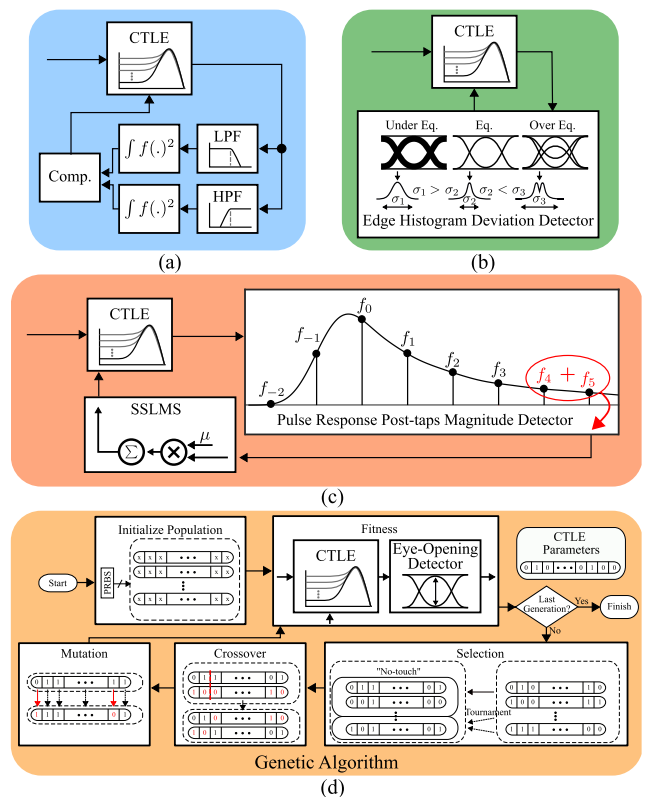

FIGURE 2. Representative methods of available CTLE adaptation techniques. (a) Comparison of low and high-frequency magnitudes using filters and integrators [10], (b) Measurement of eye edge transitions standard deviation through signal transition oversampling [11], (c) Minimization of the sum of f_4 and f_5 post-taps using SSLMS adaptation [12] and (d) Genetic algorithm with a fitness function based on eye-opening [13].

the CTLE source resistance. In [13], a complete receiver front-end adaptation is presented which calibrates multiple parameters through a genetic algorithm by taking the receiver eye-opening as the error function as shown in Fig. 2(d). The genetic algorithm is beneficial to find a good solution to the
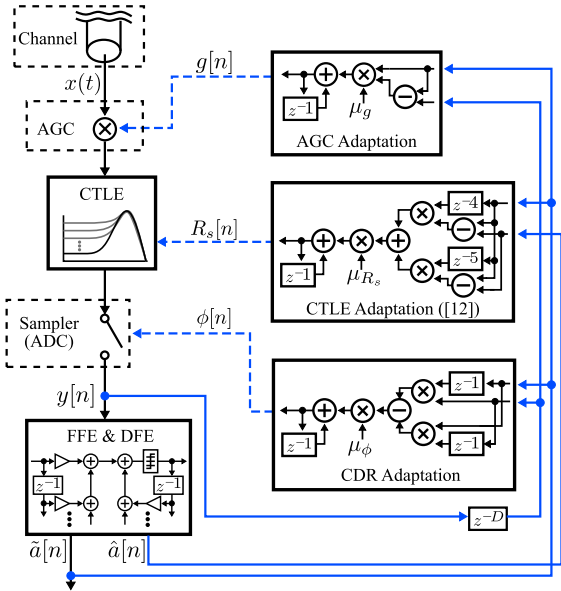
FIGURE 3. Block diagram representation of the receiver main adaptation loops and data path.

complicated multi-parameter problem. However, the genetic algorithm may be unreliable for background calibration during some error function checking points as it needs to visit many solutions far from optimal.

This paper proposes a multiple CTLE background calibration that can concurrently tune the source resistance and capacitance of short and long-tail CTLEs. The proposed method is ADC-DSP-based receiver-friendly as it utilizes multiple ISI tap estimations. Therefore, multiple calibration degrees of freedom can be achieved. The error estimation hardware has a similar logic to conventional Mueller-Muller adaptation methods. Hence, the hardware complexity is greatly alleviated as in [12]. The developed method considers the interaction with multiple receiver building blocks such as AGC and CDR. In consequence, the proposed work paves the way to fully background adaptive receivers in state-of-the-art interfaces.

Section II presents the system model utilized throughout the paper with brief descriptions of the receiver's main building blocks. Likewise, Section II discusses the noise interaction between the CTLE, ADC and FFE. Section III presents the proposed adaptation algorithm for CTLEs and analyzes the multiloop interaction with the other receiver's main building blocks. A custom logic is proposed to solve the control problem between two CTLEs. Moreover, Section III presents an intuitive analogy for the proposed adaptation algorithm. Section IV validates the proposed work by showing numerical results with a wide range of real channel models. Finally, Section V concludes this article.

II. SYSTEM MODEL
Fig. 3 shows a simplified model of the receiver depicted in Fig. 1(b) along with a detailed illustration of the adaptation loops commonly employed by the state-of-the-art

publications [12], [22], [23], [24]. The received signal can be represented as [25]

$$x(t) = \sum_{k=-\infty}^{\infty} a[k]f_c(t - kT) + m_c(t), \qquad (1)$$

where $a[k]$ is a random transmitted symbol, which is assumed to be the k-th transmitted symbol, $f_c(t)$ represents the *single pulse response* of the channel where $f = (h_c * c)$ with h_c being the channel impulse response and c the linear modulator (a unit pulse) [26] defined as $c(t) = 1$ for $|t| < 1/2$ and 0, otherwise. T represents the symbol period. Likewise, $m_c(t)$ is a zero-mean Gaussian noise process, representing the diverse sources of noise such as jitter, thermal, crosstalk, etc. In a communication without ISI, $f_c(t - kT) = 0$ for all $k \neq 0$. Moreover, the received signal depends on a linear combination of the transmitted symbols $a[k]$ and the weighting factors $f_c(t - kT)$. The equalized and sampled signal can be represented as

$$y[n] = g[n]\left(\sum_{k=-\infty}^{\infty} a[k]f((n - k)T - \phi[n]) + m(nT)\right), \qquad (2)$$

where $g[n]$ is a conditioning factor representing the AGC gain control at sample n, the $f(t)$ is the result of the convolution between the channel pulse response $f_c(t)$ and the receiver CTLE controlled by the parameter $R_s[n]$, the $\phi[n]$ is the phase control of the CDR adaptation and the $m(t)$ is the simplification of all the noise sources including quantization noise. The $y[n]$ models the sampling of the ADC in the receiver. Moreover, the samples pass through the FFE/DFE for digital equalization. The structure of FFE/DFE equalization can be viewed as a combination of finite impulse response (FIR) and infinite impulse response (IIR) filters [24] as

$$\widehat{a}[n] = \sum_{k=0}^{k=\alpha-1} y[n-k]w_k[n] + \sum_{k=1}^{k=\beta} \tilde{a}[n-k]\widehat{f}_k[n]. \qquad (3)$$

Here, α, β, w_k, and $\widehat{f}_k$ represent the FFE length, DFE length, k-th estimated filter weight, and k-th estimated ISI tap after FFE correction, respectively. The $\widehat{a}$ denotes the equalized received sample before the slicer decision and $\tilde{a}$ denotes the slicer symbol decision from $\widehat{a}$. The weights of the FFE and DFE can be updated by minimizing the cross-correlation between the output sample and the error with

$$w_k[n] = w_k[n-1] + \mu_w y[n-k](\tilde{a}[n] - \widehat{a}[n]) \qquad (4)$$

and

$$\hat{f}_k[n] = \hat{f}_k[n-1] + \mu_{\hat{f}}\tilde{a}[n-k](\tilde{a}[n] - \widehat{a}[n]). \qquad (5)$$

Here, μ_w and $\mu_{\hat{f}}$ represent the adaptation weights for the FFE and DFE, respectively. The channel ISI taps before the FFE can be estimated as

$$\tilde{f}_k = E[\tilde{a}[n-k]y[n]], \qquad (6)$$

where $E[.]$ refers to the expectation operator.

In Fig. 3, the AGC gain control is simplified by a multiplication with the weight $g[n]$. In general, the AGC gain can be controlled to match the channel reference levels with the main tap (f_0) magnitude [23] as

$$g[n] = g[n-1] + \mu_g \tilde{a}[n](\tilde{a}[n] - y[n]), \quad (7)$$

where $\tilde{a}$ represents the estimated symbol sequence, μ_g the gain adaptation coefficient. Furthermore, the CDR is responsible for estimating the eye center sampling position for the ADC. The dominant approach for phase control on baud rate receivers is the Mueller-Muller logic [22] due to its simplicity and fast adaptation. The Mueller-Muller phase detector (MMPD) minimizes the difference between the pre-tap (f_{-1}) and the post-tap (f_1) as

$$\phi[n] = \phi[n-1] + \mu_\phi(y[n]\tilde{a}[n-1] - y[n-1]\tilde{a}[n]), \quad (8)$$

where ϕ represents the ADC sampling phase and μ_ϕ represents the phase adaptation step. The MMPD does not guarantee the sampling phase with the smallest ISI conditions. However, the MMPD remains a highly efficient method that can yield acceptable results. Dual-loop ADC-DSP based receivers with independent digital equalization paths have been proposed to achieve both effective equalization and reduced loop latency for improved JTOL [5], [6], [20]. Alternatively, it is also possible to estimate the CDR taps directly from the ADC output [27], [28], [29]. Fig. 3 also shows the adaptation loop employed by [12]. The CTLE source resistance is updated by estimating the summation of the post-taps $\hat{f}_4$ and $\hat{f}_5$ as

$$\begin{aligned} R_s[n] = R_s[n-1] &+ \mu_{R_s}\big(\tilde{a}[n-4](\hat{a}[n] - \tilde{a}[n]) \\ &+ \tilde{a}[n-5](\hat{a}[n] - \tilde{a}[n])\big), \end{aligned} \quad (9)$$

where μ_{R_s} is the adaptation step of R_s and $\hat{a}[n]$ is utilized instead of $y[n]$ because [12] takes into account the DFE equalization for the update of the CTLE. In [12] there is no FFE ($\alpha = 0$) and a single tap DFE is employed ($\beta = 1$). The update of the CTLE weight can also use the output of the ADC directly to avoid loop interactions with the digital equalization. The limitation of [12] lies in the control of a single parameter (R_s) for a single CTLE in the receiver. Furthermore, the CTLE and channel model will be discussed in more detail.

A. CTLE MODEL

Fig. 4(a) illustrates the most common implementation of a CTLE [5], [6], [30]. The frequency response of the CTLE can be represented as

$$CTLE(s) = \frac{g_m(\frac{1}{C_s R_s} + s)}{C_l(\frac{1}{C_l R_l} + s)(\frac{1 + g_m R_s}{C_s R_s} + s)}, \quad (10)$$

where R_l, C_l, R_s, C_s and g_m stand for the load resistance, load capacitance, source resistance, source capacitance and transconductance, respectively. In Fig. 4(b), the frequency response of the CTLE is shown by varying both C_s and R_s. The DC gain and the amount of high-frequency peaking are
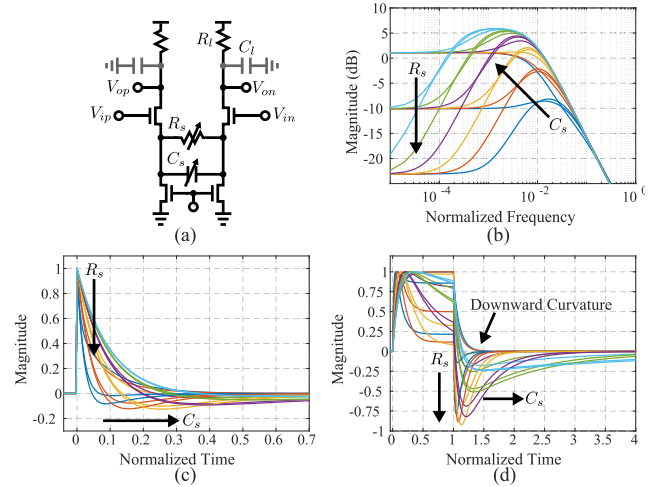

FIGURE 4. (a) A common CTLE implementation with programmable degeneration resistance and capacitance. (b) The CTLE frequency response when varying the source resistance and capacitance. (c) The CTLE impulse response when varying the source resistance and capacitance and (d) the CTLE pulse response when varying the source resistance and capacitance.

controlled by R_s. On the other hand, C_s determines the start of the roll-off frequency by shifting a zero-pole pair to the left. Another CTLE tuning method involves adjusting both C_s and C_l to alter the high-frequency power without decreasing the DC gain [3]. Unfortunately, tuning the load capacitance introduces parasitic overhead from the configurable scheme, which ultimately degrades the achievable bandwidth.

The impulse response of (10) is defined as

$$h_e(t) = \frac{g_m\left(e^{-\frac{t}{C_l R_l}}\left(R_l - \frac{C_s R_s}{C_l}\right) + g_m R_l R_s e^{-\frac{g_m R_s t + t}{C_s R_s}}\right)}{C_l(g_m R_l R_s + R_l) - C_s R_s} \quad (11)$$

for $t > 0$. Fig. 4(c) displays the CTLE impulse response for different values of C_s and R_s. Each obtained impulse response is normalized by its maximum magnitude. Similarly, Fig. 4(d) shows the CTLE pulse response, with each obtained pulse normalized by its maximum magnitude. It is noticeable that increasing the R_s creates a downward curvature in the pulse response while increasing the C_s shifts the curvature to the right. The mentioned downward resembles a negative Gaussian shape that starts after the normalized time 1 in Fig. 4(d) as will be discussed later. A normalized time unit can be seen as a unit interval of the symbol period. The observed effect between Fig. 4(c) and Fig. 4(d) are consistent with the changes in C_s and R_s. Moreover, advanced receivers can incorporate a second CTLE with larger C_s to address far ISI taps from the main tap.

B. CHANNEL MODEL

The ideal representation of the channel is based on the concept of a transmission line [32], using a specific set of physical parameters. However, a complexity challenge arises when dealing with practical channels that often comprise multiple sections with distinct characteristics. To address
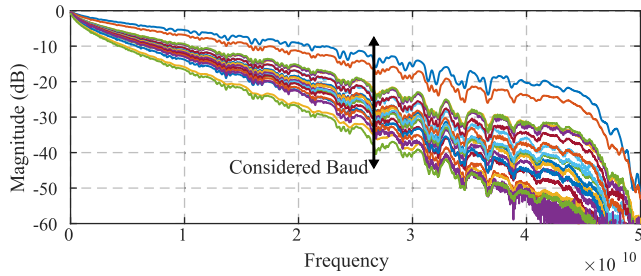
FIGURE 5. Traditional backplane channel frequency responses [4] along with the considered baud frequency throughout this paper.
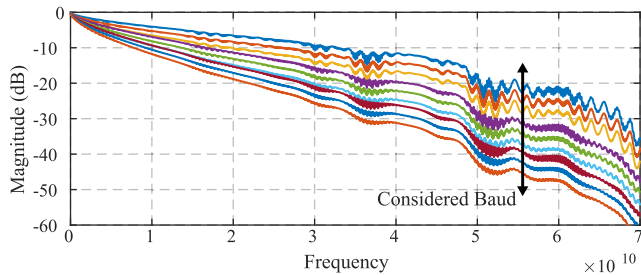

FIGURE 6. Prototype backplane channel frequency responses terminated by via [31] along with the considered baud frequency throughout this paper.

this, alternative approaches can be considered. One approach involves simplifying the channel model by using single-pole pulses, Gaussian pulses, or fourth-order Bessel-Thompson pulses [33], [34]. Another practical approach is to utilize real-world channel models, which provide a diverse range of options for incorporation into simulation environments. Fig. 5 shows the frequency response of traditional backplane channels with various insertion loss configurations [4]. The considered baud rate throughout the paper is also shown. Likewise, Fig. 6 shows the frequency response of prototype backplane channels with various insertion loss configurations [31] having via terminations. These realistic channel models enable an accurate analysis of the channels behavior and facilitate comprehensive evaluations of the system's performance.

C. CTLE-ADC-FFE NOISE
The FFE amplifies the incoming noise from the input path and the ADC quantization noise proportionally to the ISI magnitude. In (3), the noise-dependent factors can be discriminated as

$$\widehat{a}'[n] = \sum_{k=0}^{\alpha-1} (m_e[n-k] + q[n-k])w_k[k], \qquad (12)$$

with m_e and q being the CTLE shaped noise and ADC quantization noise, respectively. The noise relationship between the CTLE, ADC and FFE is summarized by (12). There are two main noise terms, $m_e w_k$ and $q w_k$. The CTLE-shaped noise m_e is amplified by the FFE weights w_k in the same way as the ADC quantization noise q. As the CTLE equalization

increases, m_e will become larger while w_k smaller and vice versa. Hence, the $m_e w_k$ product can be seen as constant. On the other hand, if the CTLE equalization is poor, the FFE equalization needs to be improved (increased weights w_k), which will increase the $q w_k$ product. Therefore, the best equalization noise scenario is when the CTLE minimizes the input ISI as much as possible because $m_e w_k$ can be considered constant while the ADC quantization noise q is amplified by the magnitude of the FFE weights in the $q w_k$ product. In consequence, observing the ADC output directly (without FFE/DFE) is sufficient to update the CTLE parameters for the receiver noise optimization.

III. PROPOSED CTLE ADAPTATION
A. PROPOSED CTLE ADAPTATION INTUITION
As previously discussed in Fig. 4(d), tuning the CTLE R_s and C_s is analogous to shaping a downward curvature in the pulse response. Consider, a negative Gaussian-like function to intuitively represent the CTLE downward curvature as

$$h'_C(t) = -R_s e^{-(t-\gamma C_s)^2/C_s}, \qquad (13)$$

where γ is an offset factor proportional to C_s. In Fig. 4(d), it is possible to observe that increasing R_s increases the depth of the curvature while C_s shift and spread the curvature at the same time. Hence, (13) is built accordingly. γC_s in (13) shift the curvature offset when C_s is changed while C_s changes the downward curvature width. On the other hand, R_s changes the curvature depth. All of this control behavior is targeted to resemble the downward curvature in Fig. 4(d) when C_s and R_s are changed. Likewise, in this analogy, γ would be defined by the CTLE specifications. Fig. 7(a) illustrates (13) when varying C_s and R_s with $\gamma = 1$. The equalization problem function can also be simplified as

$$J(t) = e^{-\rho t} + h'_C(t), \qquad (14)$$

where $J(t)$ denotes the error function. A decaying exponential is added to imitate the effect of ISI and ρ is the decaying factor. In (14), the summation operation between the decaying exponential and the analogous CTLE response is selected to further simplify the analysis and intuition. The decaying exponential is only imitating the pulse response post-taps region which is the target of the proposed adaptation.

Section II explains that the estimated main tap magnitude ($\tilde{f}_0$) can be used as a direction for the AGC gain control. Likewise, the difference between the pre and post-tap ($\tilde{f}_1 - \tilde{f}_{-1}$) is the well-known error function for the Mueller-Muller phase adaptation method. Moreover, this paper proposes that the taps information can also be used for the adaptation of multiple CTLEs. For instance, the cancellation of two post-taps can be represented by making $J(t_1) = 0$ and $J(t_2) = 0$, where t_1 and t_2 are two arbitrary time positions. The solution for R_s and C_s is given as

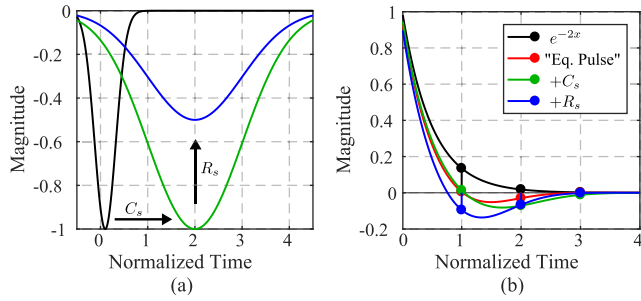$$R_s = e^{-\rho t_1 + ((t_1 - \gamma C_s)^2)/C_s} \qquad (15)$$

FIGURE 7. (a) The analogous function behavior when varying R_s and C_s parameters resembling the downward curvature in Fig. 4(d) and (b) the analogous equalization utilizing a decaying exponential to mimic ISI effects. The pulse is equalized by zeroing $J(1)$ and $J(3)$.

and

$$C_s = (t_1 + t_2)/(\rho + 2\gamma). \quad (16)$$

Fig. 7(b) shows the analogous equalization to make $J(1)$ and $J(3)$ zero by selecting a specific R_s and C_s pair. Likewise, Fig. 7(b) shows (14) when varying both R_s and C_s from the equalized solution. The obtained results are an analogy of the convolution between the channel pulse response and the CTLE impulse response for a simpler observation of the proposed adaptation operation. Hence, the presented analogy is an intuitive means of explanation with relaxed accuracy. The following subsections will further develop the proposed CTLE adaptation theory considering the multiple receiver loops and a more precise numerical analysis.

B. SINGLE CTLE ADAPTATION

The proposed adaptation of R_s and C_s for a single CTLE is defined with a LMS logic as

$$R_s[n] = R_s[n-1] + \mu_{R_s}(\tilde{a}[n-1](y[n] - \tilde{a}[n])) \quad (17)$$

and

$$C_s[n] = C_s[n-1] + \mu_{C_s}(\tilde{a}[n-3](y[n] - \tilde{a}[n])). \quad (18)$$

where μ_{C_s} is the adaptation step of C_s. Hence, the update of R_s will force $\tilde{f}_1$ to zero and the update of C_s will force $\tilde{f}_3$ to zero. Furthermore, the reliability of the proposed adaptation is discussed in this subsection.

Fig. 8(a) shows the single pulse response of a single CTLE being convolved with a traditional backplane channel [4] having an approximate insertion loss of 24 dB at Nyquist for multiple values of R_s and C_s. The single CTLE impulse response is given by (11) with parameters absolute values $g_m = 0.4\ mS$, $R_l = 50\Omega$ and $C_l = 2mF$. The parameters are chosen to work with time units of 1 (CTLE gain peaking at the Nyquist frequency) for simplicity and without loss of generality. Moreover, each obtained single pulse response is phase shifted to make the main tap $\tilde{f}_0$ at time position 0 considering the Mueller-muller phase reference and the pulse response is scaled to make the main tap equal to 1 as the AGC would employ. Fig. 8(b) shows the single pulse response that returned the smallest magnitude for the combined absolute
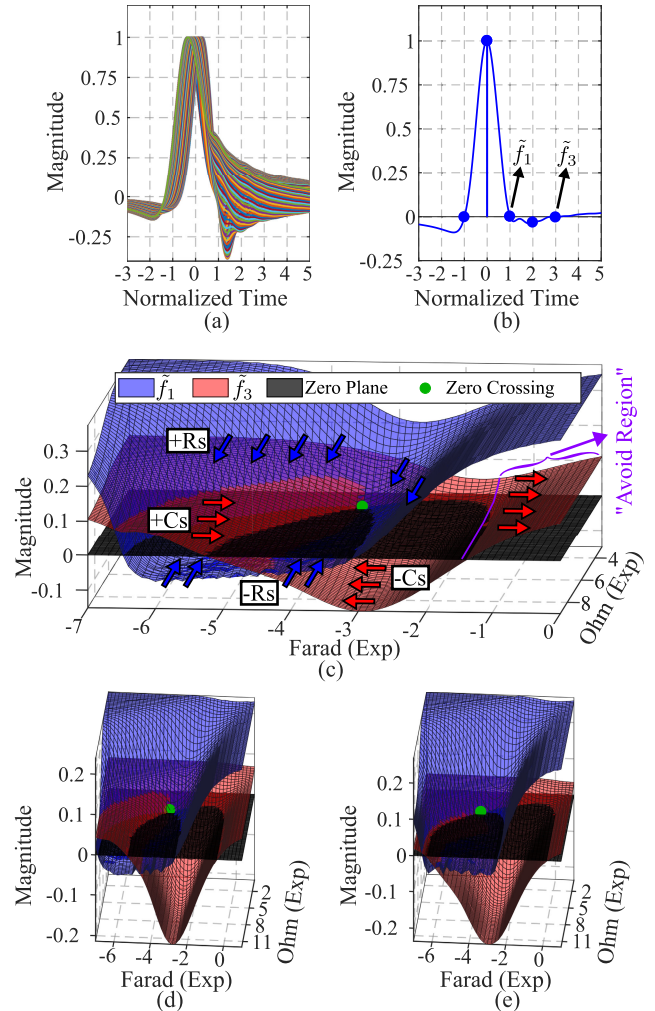

FIGURE 8. (a) The single pulse response of a single CTLE being convolved with a traditional backplane channel [4] having an approximate insertion loss of 24 dB at Nyquist for multiple values of R_s and C_s. (b) The pulse response that returned the smallest magnitude of the combined absolute values of $\tilde{f}_1$ and $\tilde{f}_3$ when the values of R_s and C_s are swept. (c) The surfaces of $\tilde{f}_1$ and $\tilde{f}_3$ by varying R_s and C_s with exponential steps along with the zero plane and a point to indicate where $\tilde{f}_1$ and $\tilde{f}_3$ meet and are equal to zero. The LMS update direction of the parameters is highlighted with arrows and an "avoid region" is shown where the adaptation can lose the sense of direction. (d) The same surface plot for a prototype backplane channel with approximately 25 dB insertion loss and (e) for a one-pole channel.

values of $\tilde{f}_1$ and $\tilde{f}_3$ when the values of R_s and C_s are swept. Furthermore, Fig. 8(c) shows the surfaces of $\tilde{f}_1$ and $\tilde{f}_3$ by varying R_s and C_s with exponential steps along with the zero plane and a point to indicate where $\tilde{f}_1$ and $\tilde{f}_3$ meet and are approximately zero. The key point to observe from Fig. 8(c) is how an LMS algorithm would behave if R_s is controlled to make $\tilde{f}_1 = 0$ and C_s is controlled to make $\tilde{f}_3 = 0$. The update sign of R_s and C_s will depend on whether $\tilde{f}_1$ and $\tilde{f}_3$ are above or below the zero plane. Furthermore, Fig. 8(c) includes arrows pointing to the update direction of the parameters for a given R_s and C_s value pair for each surface. It is possible to observe that the parameters would be able to find the zero crossing location except if the parameters value pair

enters the "avoid region", where the update of C_s would wrongly change the sign of update and could continually go in the wrong direction. The mentioned update failure can happen if the C_s value becomes too high (above e^{-2} Fig. 8(c)). The analyzed behavior can be directly addressed to a wide range of channels. For instance, Fig. 8(d) and Fig. 8(e) plot the surfaces for a prototype backplane channel with approximately 25 dB insertion loss and for a one-pole channel, respectively. The exponential channel impulse response is modeled as e^{-t} for $t > 0$. The "avoid region" can also be explained by considering that if the C_s value becomes too high, the downward curvature depth caused by R_s decreases until it is not capable of zeroing the post-taps. Such behavior can also be seen in Fig. 4(d). The simplest way to avoid the "avoid region" is to limit the maximum value of C_s based on the CTLE response. The CTLE might not be able to equalize the near taps such as $\tilde{f}_1$ if it is heavily band-limited or the channel loss is greatly high. The bandwidth limits the roll-off speed in (11) and consequently the near taps equalization capability. The utilized taps for CTLE update could be changed for farther taps in order to overcome possible bandwidth limitations of the system.

The concurrent LMS update of R_s and C_s will be numerically analyzed for further verification of the proposed adaptation algorithm. Fig. 9(a) shows a linear version of the 4×4 multiloop system [35] with the AGC, CTLE R_s, CTLE C_s and CDR. The parameters C_s and R_s are initially tuned by considering $\tilde{f}_1$ and $\tilde{f}_3$, respectively. Fig. 9(a) input and output relationship can be mathematically represented as

$$\underbrace{\begin{bmatrix} Y_1 \\ Y_2 \\ Y_3 \\ Y_4 \end{bmatrix}}_{\boldsymbol{Y}} = \underbrace{\begin{bmatrix} G_1 & \phi_1 & C_{s1} & R_{s1} \\ G_2 & \phi_2 & C_{s2} & R_{s2} \\ G_3 & \phi_3 & C_{s3} & R_{s3} \\ G_4 & \phi_4 & C_{s4} & R_{s4} \end{bmatrix}}_{\boldsymbol{K}} \underbrace{\begin{bmatrix} U_1 \\ U_2 \\ U_3 \\ U_4 \end{bmatrix}}_{\boldsymbol{U}}, \tag{19}$$

where G_i is the AGC open loop transfer function from the manipulated variable U_i to the controlled variable Y_i. Because there are four controlled variables and four manipulated variables, sixteen process transfer functions are necessary to completely characterize the system dynamics. C_{si}, R_{si} and ϕ_i represent the CTLE C_s, CTLE R_s and Mueller-Muller open loop transfer functions, respectively. Likewise, G_{ci} and E_i are the i-th controller transfer function and output error, respectively. In Fig. 9(a), the input and output are paired for the AGC gain control G (U_1) and $\tilde{f}_0$ (Y_1), the Mueller-Muller phase control ϕ (U_2) and $\tilde{f}_1 - \tilde{f}_{-1}$ (Y_2), the CTLE source capacitance control C_s (U_3) and $\tilde{f}_1$ (Y_3) and the CTLE source resistance control R_s (U_4) and $\tilde{f}_3$ (Y_4). Note that the input and output pair for the CTLE source resistance and capacitance are chosen arbitrarily at first. In the multi-loop system, it is desirable to obtain quantitative information about the loops interaction and the input and output pairs for best controllability. For example, it is desirable to know if it would be better to control $\tilde{f}_3$ with C_s and vice-versa. In [35] and [36], Bristol's Relative Gain Array (RGA) method is described for

the analysis of multivariate control problems. The method only requires the steady-state gain matrix of the system $\boldsymbol{K}$. In (19) $\boldsymbol{K}$ can be obtained by taking the steady-state gain of the open loop transfer functions. G_i is directly obtained, while ϕ_i, C_{si} and R_{si} are non-linear systems. Consequently, the steady-state gain of the multiple non-linear transfer functions can be acquired by taking the derivative at the steady-state condition of the system. Fig. 9(b) shows the pulse response of a 41dB loss at the Nyquist channel [4]. Moreover, the pulse response is equalized to make $\tilde{f}_0 = 1$ and make the remaining errors $\tilde{f}_1 - \tilde{f}_{-1}$, $\tilde{f}_1$ and $\tilde{f}_3$ equal to zero by tuning the AGC, CDR and CTLE parameters presented in Fig. 9(a). Fig. 9(b) shows the pulse responses and taps obtained by varying C_s, R_s and ϕ. The steady-state gains are obtained by numerically checking the variation of the taps when changing the input parameters. For instance, the steady-state gain of the MMPD $\phi_2 = K_{2,2}$ can be obtained as [20]

$$K_{2,2} = \frac{\Delta(\tilde{f}_1 - \tilde{f}_{-1})}{\Delta \phi}, \tag{20}$$

with Δ being a small variation applied numerically. The complete steady-gain matrix for the above pulse response is configured as

$$\boldsymbol{K} = \begin{bmatrix} 1 & 0.44 & -0.01 & 0.03 \\ 0 & 1.10 & -0.05 & 0.13 \\ 0 & 0.32 & -0.03 & 0.11 \\ 0 & -0.01 & 0.06 & 0.05 \end{bmatrix}. \tag{21}$$

The relative gain matrix can be calculated by $\boldsymbol{\lambda} = \boldsymbol{K} \odot (\boldsymbol{K}^{-1})^T$ where $\odot$ stands for the element-wise multiplication. The calculated relative gain matrix is presented as

$$\boldsymbol{\lambda_1} = \begin{array}{c} \\ Y_1(\tilde{f}_0) \\ Y_2(\tilde{f}_\phi) \\ Y_3(\tilde{f}_1) \\ Y_4(\tilde{f}_3) \end{array} \begin{array}{cccc} U_1(G) & U_2(\phi) & U_3(C_s) & U_4(R_s) \\ \begin{bmatrix} 1 & 0 & 0 & 0 \\ 0 & 1.56 & -0.14 & -0.42 \\ 0 & -0.06 & 0.33 & 1.22 \\ 0 & 0 & 0.81 & 0.19 \end{bmatrix}, \end{array}$$

$$\tag{22}$$

where $\tilde{f}_\phi = \tilde{f}_1 - \tilde{f}_{-1}$. The above matrix rows are labeled with their respective outputs while the columns are labeled with their respective inputs. The relative gain matrix $\boldsymbol{\lambda}$ can give a measure of process interactions and a recommendation for the most effective pairing of controlled and manipulated variables [35]. The advantage of $\boldsymbol{\lambda}$ is that it is not affected by the scaling of the variables since it is a relative matrix and each row and each column sum to one. Therefore, it can capture the essence of the process. In short, as a value in the relative gain matrix $\lambda_{i,j}$ reaches zero, the relationship between the input-output pair of that row-column becomes weaker, with it being completely independent if it reaches zero. On the other hand, if the lambda value is too high, the interaction of that input to other outputs is severe which degrades the controllability of the multiple-input multiple-output (MIMO) system. Hence, the ideal control condition is when a row has a single $\lambda_{i,j} = 1$ which implies that closing the other

loops does not affect the current input-output relationship. The RGA method recommends pairing the controlled and manipulated variables so that corresponding relative gains are positive and as close to one as possible. Consequently, in (22), Y_1 should be paired with U_1 and Y_2 with U_2 as expected. However, the RGA recommends that Y_3 be paired with U_4 instead of U_3 and Y_4 be paired with U_3 instead of U_4. Thus, the proposed CTLE adaptation method for a single CTLE considers the pairs $Y_3 - U_4$ and $Y_4 - U_3$ for the update of $\tilde{f}_1$ and $\tilde{f}_3$ taps. The change of input and output pairs can be accomplished by changing the output errors as illustrated in Fig. 9(a). In (22), the paired values are close to one. Hence, the input and output pairs have a significant degree of independence. Performing the same analysis considering the taps $\tilde{f}_2$ and $\tilde{f}_3$ for R_s and C_s, respectively returns lambda values closer to one (better control) but the equalization performance (remaining ISI) is worse when verified through simulations. One should note that the RGA analysis developed here is related to the convergence behavior of the parameters and not directly related to the final ISI cancelation result. Various methods for the stability analysis of multiloop systems are presented in [35]. The current loops stability problem can be treated as single-loop systems since they have a good level of independence. In addition, the dynamic behavior of the system is verified with numerical simulations in Section IV.

C. MULTIPLE CTLE ADAPTATION

The presented adaptation theory can be expanded to the case of two CTLEs as illustrated in Fig. 1(b). Thus, a 6×6 MIMO system relative gain matrix can be constructed by looking into the pulse response of Fig. 9(b) utilizing two CTLEs with the relative gain matrix as

$$\lambda_2 =$$

$$
\begin{array}{c}
\\
(\tilde{f}_0) \\
(\tilde{f}_\phi) \\
(\tilde{f}_1) \\
(\tilde{f}_3) \\
(\tilde{f}_4) \\
(\tilde{f}_5)
\end{array}
\begin{array}{c}
\begin{array}{cccccc}
(G) & (\phi) & (R_H) & (C_H) & (R_M) & (C_M)
\end{array} \\
\left[
\begin{array}{cccccc}
1 & 0 & 0 & 0 & 0 & 0 \\
0 & 1.98 & 2.39 & -0.21 & -2.11 & -1.05 \\
0 & -0.99 & -6.56 & 0.27 & 5.31 & 2.98 \\
0 & -0.04 & 18.88 & 0.95 & -26.01 & 7.22 \\
0 & 0.06 & -37.94 & 2.30 & 62.17 & -25.59 \\
0 & -0.01 & 24.23 & -2.31 & -38.35 & 17.44
\end{array}
\right],
\end{array}
$$

(23)

where a high-frequency CTLE is controlled by a source resistance R_H and source capacitance C_H and a middle-frequency CTLE is controlled by a source resistance R_M and source capacitance C_M. The obtained relative gain matrix in (23) has values that are much bigger than 1. Hence, even if each row and column can be paired with a non-negative number, the MIMO system has poor controllability. In other words, turning on all the loops at the same time is nearly unfeasible. Performed simulation results have also shown difficulty with the presented 6×6 MIMO system.

A custom sequential logic was developed in order to overcome the poor controllability presented in (23) when
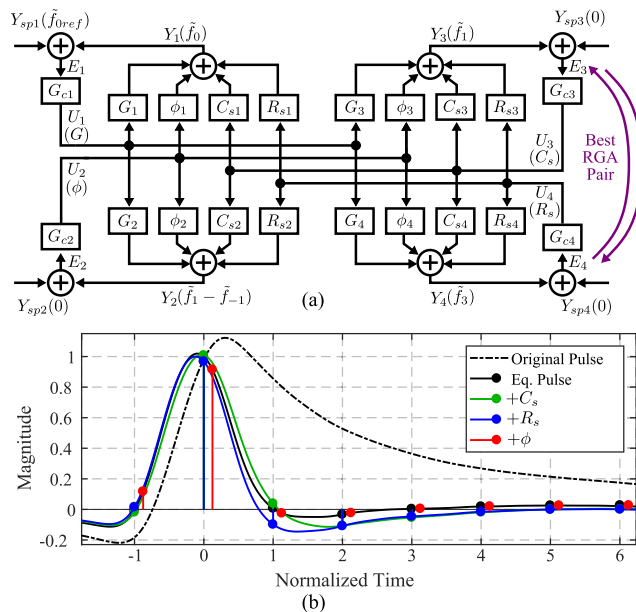

FIGURE 9. (a) Linear version of the 4×4 multiloop system with the receiver AGC, CTLE R_S, CTLE C_S and CDR represented in Fig. 1(a) and (b) the pulse responses and taps by varying C_S, R_S and ϕ to obtain the steady-gain matrix K for the RGA analysis.

two CTLEs are controlled simultaneously. Fig. 10(a) shows the proposed logic fluxogram representation which can be incorporated with a state machine. Likewise, Fig. 10(b), Fig. 10(c), Fig. 10(d) and Fig. 10(e) illustrate the steps of the proposed algorithm. In the first stage, the mid-CTLE R_M and C_M are updated by forcing $\tilde{f}_4$ and $\tilde{f}_5$ to zero, respectively as shown in Fig. 10(b). This loop repeats until a given number of iterations. Furthermore, the mid-CTLE retreat state decreases R_M and C_M until all of the analyzed post-taps from $\tilde{f}_1'$ to $\tilde{f}_5'$ are non-negative and $\tilde{f}_2' > \tilde{f}_3'$ as shown in Fig. 10(c). The retreat is necessary because if a CTLE is at the minimum code, it cannot reverse the equalization of the other CTLE. Likewise, $\tilde{f}_2' > \tilde{f}_3'$ is necessary to recover the pulse response smoothness and resemble the condition observed in (22) for sustaining good adaptation control. After the mid-CTLE retreat, the high-CTLE R_H and C_H are updated by forcing $\tilde{f}_1$ and $\tilde{f}_3$ to zero, respectively as shown in Fig. 10(d). The high-CTLE adaptation can go on until a new cycle is triggered. If so, the high-CTLE needs to turn the post-taps non-negative in the retreat stage in order to guarantee the mid-CTLE adaptation operation as shown in Fig. 10(e). Therefore, the processes of updating the mid-CTLE and high-CTLE are similar, differing only on the calibrated coefficients and the observed taps.

Fig. 11 shows the block diagram of the proposed CTLE adaptation in the receiver. In essence, all of the adapted parameters are addressed to an ISI tap. Nevertheless, the CTLEs parameters need additional treatment to operate properly. The proposed adaptation method does not guarantee the optimum equalization configuration of the CTLEs. In contrast, it is a simple and practical approach that can lead
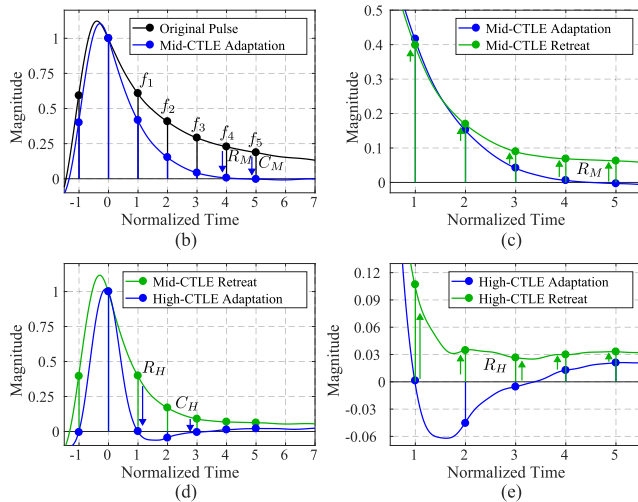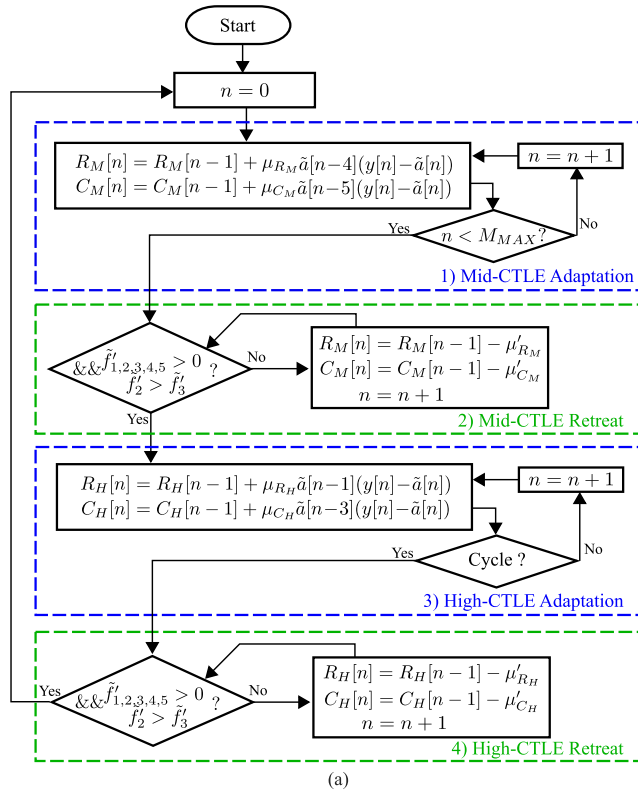
FIGURE 10. (a) The proposed multiple CTLE logic fluxogram, (b) the illustration of the middle CTLE update, (c) the illustration of the middle CTLE retreat stage, (d) the illustration of the high CTLE update and (e) the illustration of the high CTLE retreat stage.
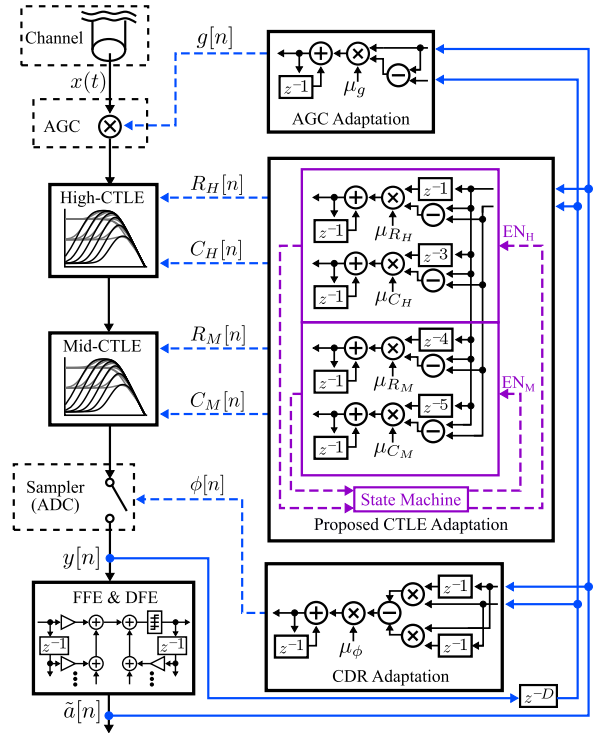

FIGURE 11. Block diagram representation of the proposed CTLE adaptation with the other receiver main building blocks. The proposed CTLE adaptation utilizes the information of the ISI taps similarly to the update of the AGC gain and CDR phase.

simulations but one might prefer a different set of taps to control the CTLE with bandwidth and equalization trade-offs. The presented concept with more than two CTLEs could be explored by following similar control methods. Although this paper focuses on DSP-based receivers, an analog-based adaptation system can be built with the presented method. For instance, the magnitude of the channel taps can be estimated in the analog domain with low-pass filters and compared with comparators.

IV. RESULTS

The results are obtained through the MATLAB environment. The simulation model includes the main building blocks described in Section II such as the AGC, CTLEs, CDR, FFE, DFE and the corresponding adaptation loops. The system is implemented with object-oriented programming to ease its realization and debugging. The selected environment and coding style provide a good tradeoff between simulation speed and code simplicity. The FFE length is set to 31 and the DFE as 1 to resemble published receivers [3], [5], [6], [37]. The FFE/DFE are updated faster than the CTLE to minimize the BER variation during the CTLE adaptation. Furthermore, the assumed CTLE parameters absolute values from (10) are $g_m = 0.5 \ mS$, $R_l = 50\Omega$ and $C_l = 0.6 \ mF$. The CTLE parameters are selected to provide a frequency peaking at the target baud rate Nyquist frequency assuming a normalized time for simplicity. In addition, R_s and C_s are

to satisfactory results as the Mueller-muller phase detection method discussed in Section II. For the first CTLE, the $\tilde{f}_1$ and $\tilde{f}_3$ taps are selected for control based on multiple performed simulations. Utilizing $\tilde{f}_1$ and $\tilde{f}_2$ might not have a zero solution if the bandwidth of the system is sufficiently limited. Nevertheless, it is possible to change the controlled ISI taps in a manner that the source resistance always controls a given tap followed by the source capacitance controlling a tap farther. In this paper, the selected taps are based on performed

FIGURE 13. 14 dB insertion loss traditional backplane channel pulse response (a) before and after the proposed CTLE adaptation from Fig. 12 along with the optimal equalization code. (b) The estimated eye diagram from the CTLE output before the proposed adaptation and (c) after the proposed adaptation.
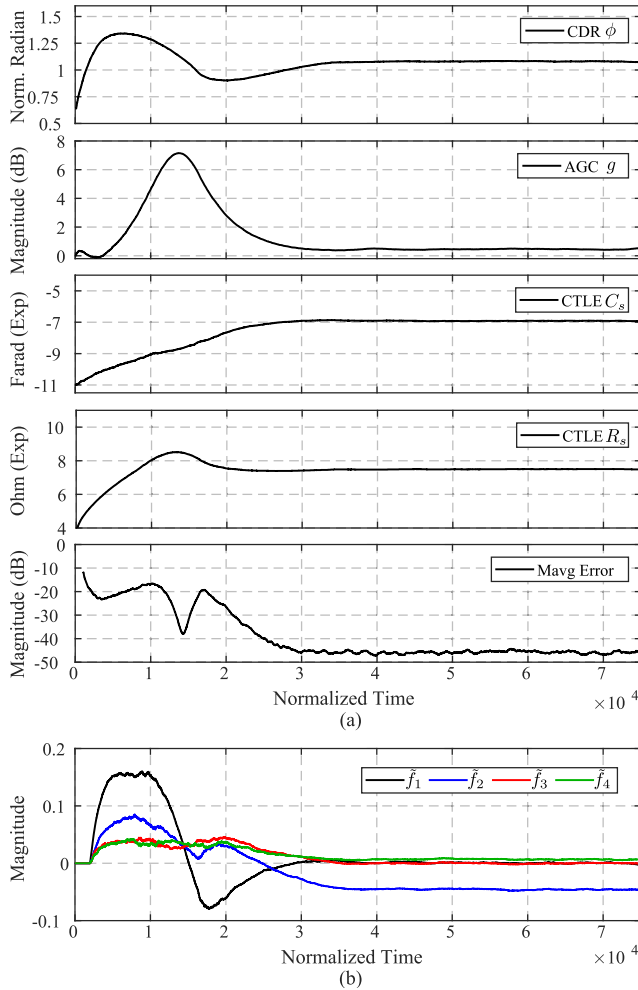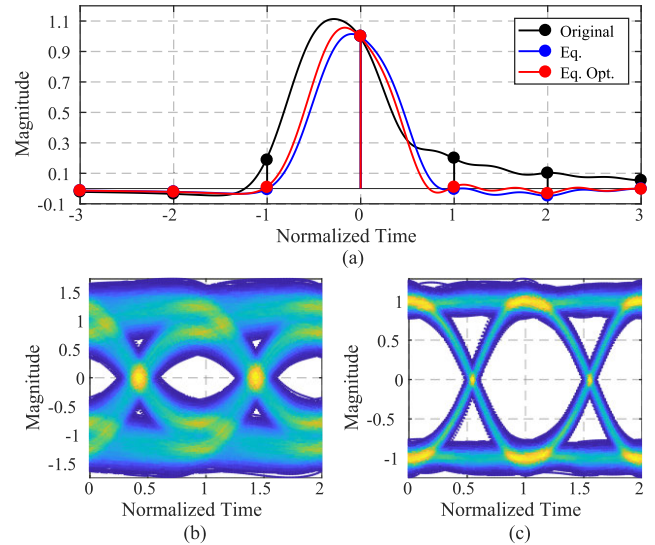
FIGURE 12. Proposed adaptation loop convergence behavior for a 14 dB insertion loss traditional backplane channel [4] showing (a) the CDR phase, AGC gain, high CTLE C_s, high CTLE R_s, the moving average error and (b) The estimated channel taps $\tilde{f}_i$ over the adaptation loop.

passed through an exponential function such as $R'_s = e^{R_s}$ before evaluating (10) to resemble the exponential steps in published receivers and increase the simulation speed. The communication is modeled as PAM-2, PAM-4 and PAM-8 transmission with signals and responses upsampled by a factor of 80 for fair convolution computation precision and reasonable simulation speed. The obtained results can also be achieved with other PAM modulations without significant differences. The selected adaptation steps for each simulation setup are set as $\mu_\phi = 0.6\ m$, $\mu_g = 0.4\ m$, $\mu_{R_H} = 2m$, $\mu_{C_H} = 4m$, $\mu_{R_M} = 4m$ and $\mu_{C_M} = 4m$. The parameters, chosen based on the observation of multiple simulation results, were carefully selected to achieve good convergence performance within a reasonable simulation time. A Gaussian noise with $\sigma = 1/(2^6)$ is added to all simulations to model the environment and ADC noises.

Fig. 12 shows the proposed adaptation for a 14 dB channel insertion loss [4] considering only the adaptation of a single CTLE R_s and C_s. Likewise, Fig. 12(a) shows the transient

of the CDR, AGC, C_s, R_s and the moving average error with $1k$ samples. In Fig. 12, the normalized radian is an angle mapping from the range $[0, 2\pi]$ to $[0, 1]$. It is possible to observe a smooth transient behavior for all the adapted parameters while the AGC has a peak due to the CTLE R_s and C_s tracking. Fig. 12(b) shows the estimated post-taps over the convergence of the parameters where both $\tilde{f}_1$ and $\tilde{f}_3$ reach zero. The presented simulation is shown to highlight the small ISI variation after convergence when a single CTLE is under adaptation. Fig. 13(a) shows the pulse response before the equalization, after the proposed equalization and after the optimal equalization. The proposed adaptation achieves a solution that is visually close to the optimum solution. Fig. 13(b) shows the estimated eye diagram for $40k$ symbols before equalization and Fig. 13(c) shows the estimated eye diagram after the proposed adaptation. The eye diagrams are taken from the CTLE output directly. Hence, the equalization effect of the FFE/DFE is not included in those plots.

The first simulation presented the proposed algorithm for a single CTLE parameters adaptation since the considered channel loss is small enough to bring a satisfactory solution with a single CTLE. Furthermore, Fig. 14(a) shows the proposed adaptation for a PAM-4 with 45 dB channel insertion loss [31] considering the adaptation of two CTLEs with parameters R_M, C_M, R_H, C_H. The retreat steps μ' are set ten times higher than the standard adaptation steps. Occasionally, depending on the channel response, the pulse response post-tap f_1 cannot be zeroed because the pre-tap f_{-1} cannot reach a negative value through equalization. For instance, consider the convolution of the CTLE impulse with the pulse response in Fig. 4 (d). Therefore, a positive non-zero threshold can be set for the minimization of f_1 to
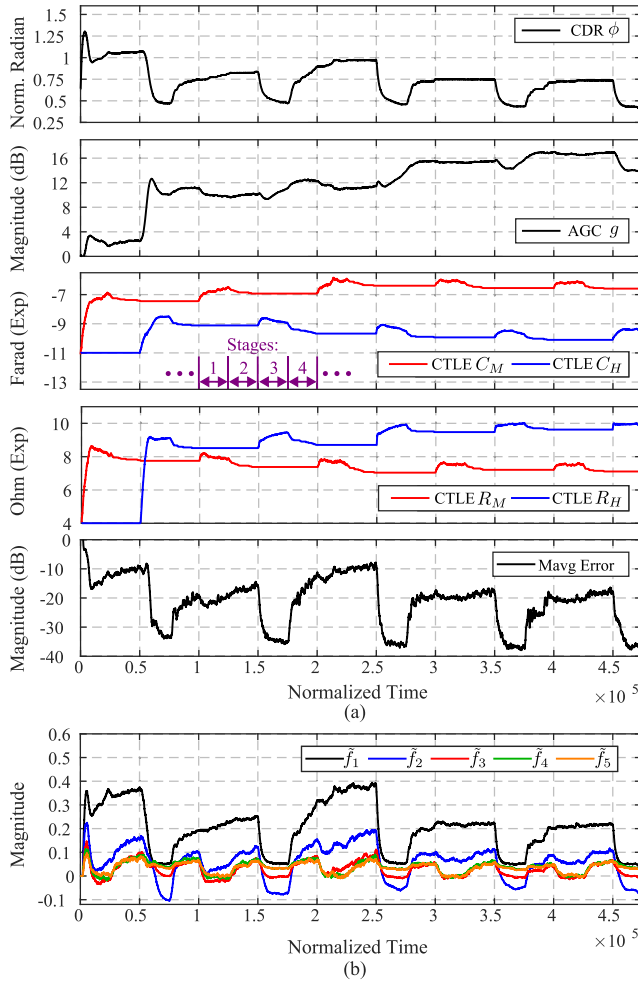
FIGURE 14. Proposed adaptation loop convergence behavior for a PAM-4 with 45 dB insertion loss prototype backplane channel [31] showing (a) the CDR phase, AGC gain, high-CTLE C_S, high-CTLE R_S, mid-CTLE C_S, mid-CTLE R_S, the moving average error and (b) The estimated channel taps $\tilde{f}_i$ over the adaptation loop.

FIGURE 15. 45 dB insertion loss prototype backplane channel pulse response (a) before and after the proposed CTLE adaptation for a PAM-4 from Fig. 14 along with the optimal equalization code. (b) The estimated eye diagram from the CTLE output before the proposed adaptation and (c) after the proposed adaptation.

enable the R_H adaptation. Here, the fixed threshold for f_1 was set to 0.05 based on simulation results observations. The CTLEs adaptation alternates between four stages as explained in Section III (Fig. 10) to enable the equalization of each CTLE while the CTLEs do not interfere with the good convergence of each other. In Fig. 14(a) a single set of the stages is highlighted with an increasing number order for better visualization of the process. Each stage is set to change every $25k$ samples. The moving average error decreases each time the proposed adaptation passes through the four stages and later stabilizes to a single set of parameter values. Fig. 14(b) shows the estimated post-taps over the parameters convergence where both f_1 and f_3 reach 0.05 and zero, respectively for a single adaptation stage while f_4 and f_5 reach zero during another adaptation stage. The current simulation result is different from the result shown in Fig. 12 in terms of ISI variation. In other words, the proposed multiple CTLE adaptation shows the best equalization performance only during a single stage of the
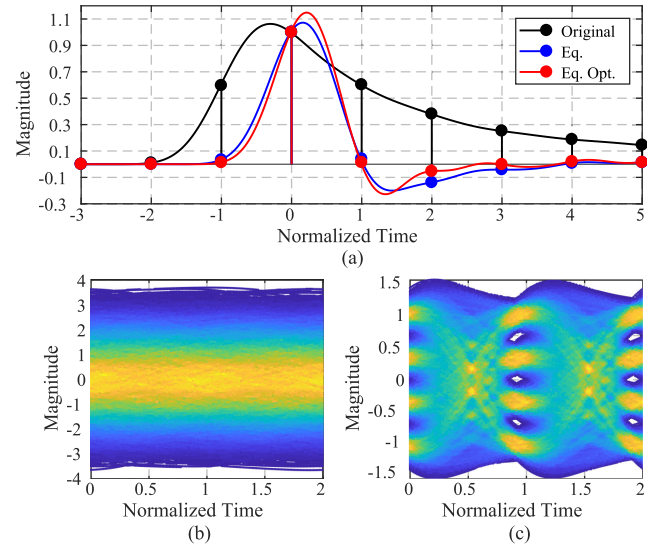
proposed adaptation. A further simulation example will show an adaptation procedure with a startup period to avoid the CTLE retreat stages. Fig. 15(a) shows the pulse response before the equalization, after the proposed equalization and after the optimal equalization considering the setup discussed in Fig. 14. The proposed adaptation achieves a solution that is visually close to the optimum solution. Fig. 15(b) shows the estimated eye diagram before equalization and Fig. 15(c) shows the estimated eye diagram after the proposed adaptation.

Fig. 16(a) shows the proposed adaptation for a PAM-8 with 35 dB channel insertion loss [4] considering the adaptation of two CTLEs with parameters R_M, C_M, R_H, C_H. Fig. 16(b) shows the estimated post-taps over the parameters convergence. The proposed multiple CTLE adaptation shows the best equalization performance only during a single stage of the proposed adaptation because the CTLE retreat stage in Fig. 10(c) and Fig. 10(e) might decrease the eye-opening (especially for the PAM-8). Likewise, during the multiple CTLE adaptation, the BER can increase to a level that the adaptation loses the sense of direction. Hence, the multiple CTLE adaptation passes through the four-stage cycles multiple times during startup with a training sequence and stops at the high CTLE adaptation. Nevertheless, new control methods could be introduced to minimize the ISI variation during the multiple CTLE adaptation stage transitions. In Fig. 16, the FFE length is increased to 61 and the DFE to 2 due to the PAM-8 tighter requirements. Fig. 17(a) shows the pulse response before the equalization, after the proposed equalization and after the optimal equalization considering the setup discussed in Fig. 16. Fig. 17(b) shows the estimated eye diagram from the
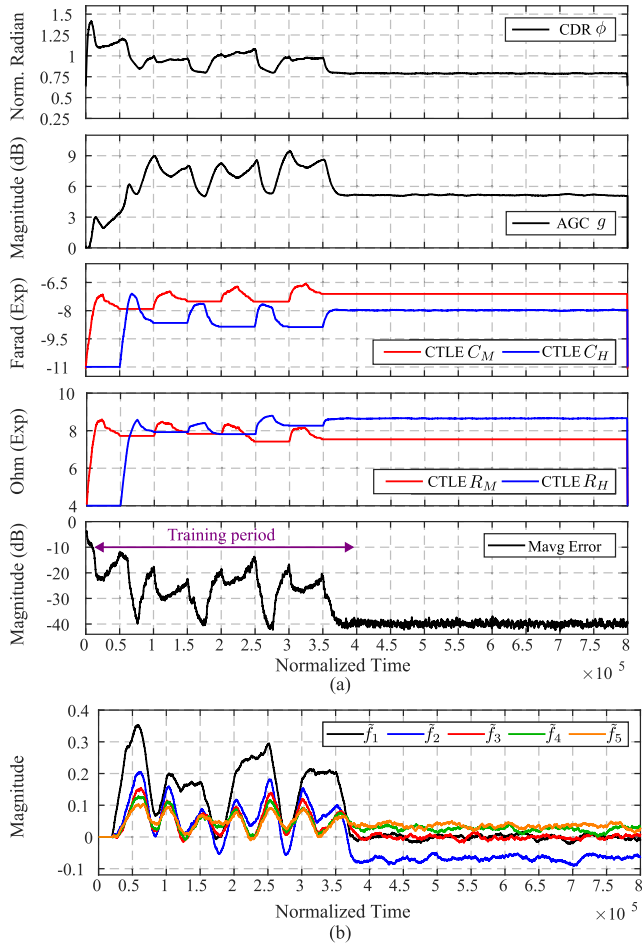
FIGURE 16. Proposed adaptation loop convergence behavior for a PAM-8 with 45 dB insertion loss traditional backplane channel [4] showing (a) the CDR phase, AGC gain, high-CTLE C_S, high-CTLE R_S, mid-CTLE C_S, mid-CTLE R_S, the moving average error and (b) The estimated channel taps $\tilde{f}_i$ over the adaptation loop. The adaptation utilizes a training sequence at the startup and later works on the background mode.
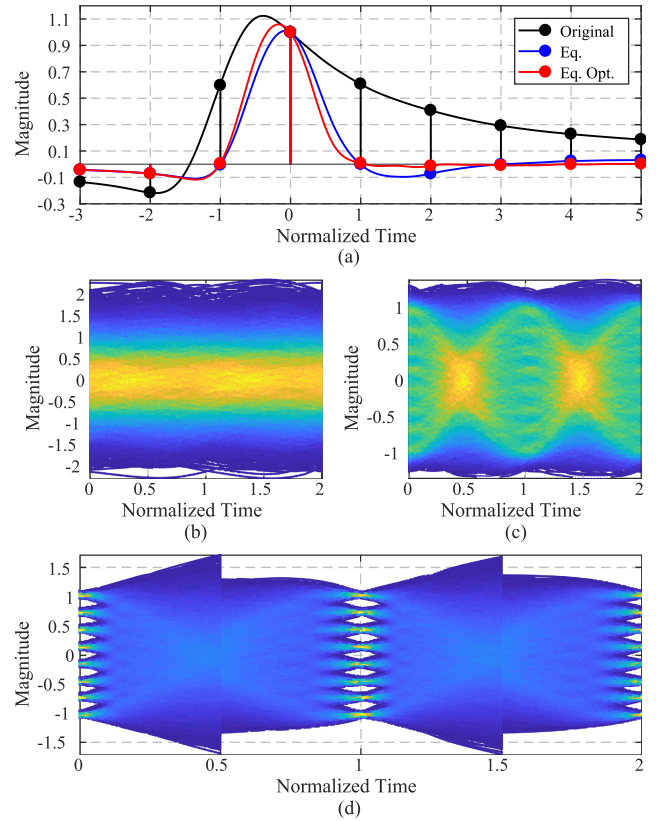

FIGURE 17. 35 dB insertion loss traditional backplane channel pulse response (a) before and after the proposed CTLE adaptation for a PAM-8 from Fig. 16 along with the optimal equalization code. (b) The estimated eye diagram from the CTLE output before the proposed adaptation. (c) The estimated eye diagram from the CTLE output after the proposed adaptation and (d) the estimated eye diagram from the FFE/DFE output.
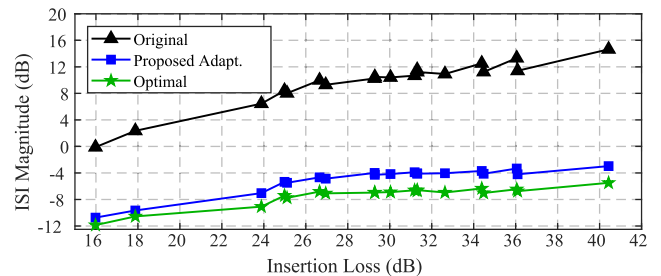

FIGURE 18. The remaining ISI magnitude before the proposed adaptation, after the proposed adaptation and after the optimal CTLEs configuration for a range of traditional backplane channel responses [4] shown in Fig. 5.

CTLE output before equalization and Fig. 17(c) shows the estimated eye diagram after the proposed adaptation. The eye is not opened at the CTLE output in Fig. 17(c) due to the high channel loss and the PAM-8 modulation, but it is possible to observe that the level lines are starting to appear after the CTLE adaptation. Furthermore, 17(d) shows the estimated eye diagram from the FFE/DFE output which would be used for the symbol decisions. The FFE/DFE eye is constructed by fixing the weights found from the MMPD phase and sweeping the sampling phase.

Fig. 18 and Fig. 19 show the proposed calibration equalization performance over different channel losses illustrated in Fig. 5 and Fig. 6, respectively. The equalization results are measured by calculating the remaining ISI magnitude (the sum of the absolute value of all taps except the main tap) when the main tap is normalized to 1. The proposed adaptation algorithm can achieve equalizations that are close to the optimal solutions with roughly a -4 dB and -8 dB degradation in the worst case for a wide range of channel

losses. Hence, different CTLE locking codes for different channel conditions in the same CTLE are presented. The results show a wide range of the equalizer adaptation.

Table 1 compares the proposed work with other CTLE adaptation techniques. The comparison items were selected to highlight the key discussion points of the presented paper with what has already been published. The disadvantages of [10], [11], [12] and [13] are discussed in Section I. In contrast with available techniques, the proposed CTLE adaptation logic is the first to directly tune the
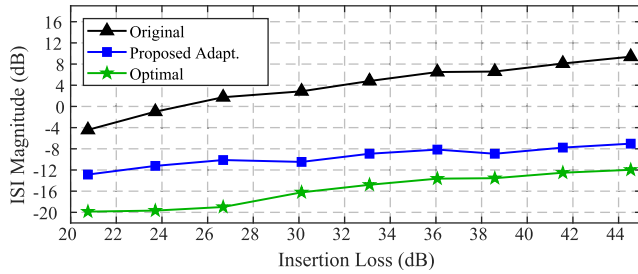
FIGURE 19. The remaining ISI magnitude before the proposed adaptation, after the proposed adaptation and after the optimal CTLEs configuration for a range of prototype backplane channel responses [31] shown in Fig. 6.

TABLE 1. Comparison with other CTLE adaptation techniques.

	This Work	[12] JSSC 2020	[13] SSC-Let 2019	[11] JSSC 2008	[10] JSSC 2006
Approach	**Back-ground[1]**	Back-ground	Fore-ground	Back-ground	Back-ground
Adaptation Logic	**Taps Mag.**	Taps Mag.	Genetic Algorithm	Eye Edge Histogram	Freq. Bands Comparison
Baud Rate	**Yes**	Yes	Yes	No	Yes
Calibration Target Parameters	$R_M, C_M,$ R_H & C_H	R_s	R_M, C_M R_H & C_H	R_s	$(R_s : C_s)^2$
Error Estimation Complexity	**Single Integrator[3]**	Single Integrator	Eye Opening	Histogram Analysis	FIR filter[4]

[1] Best performance when a single R_s and C_s pair is calibrated on background
[2] A single bias controls both R_s and C_s simultaneously
[3] For each parameter
[4] From a DSP perspective

CTLE source resistance and capacitance simultaneously and independently (to the author's knowledge). Likewise, a control adaptation is introduced to address the adaptation of multiple CTLEs parameters. However, the performance is limited for background operation when calibrating multiple sets of source capacitance and resistance. The proposed adaptation utilizes the information of the equalized channel ISI as [12] which simplifies the error estimation hardware in a similar fashion to the conventional Mueller-Muller algorithm. On the other hand, reference work might require the implementation of filters [10], calculating and performing a histogram analysis [11], or estimating the eye-opening for each iteration [13]. Moreover, the proposed work is capable of directly minimizing the first post-tap f_1 which will eventually minimize the first pre-tap f_{-1} in contrast to [12]. The potential issues, such as poor ISI during concurrent adaptation, multiloop control, and determining the CTLE C_s limit to prevent loss of convergence have been addressed.

V. CONCLUSION
This paper presents a multiple CTLE parameter adaptation suited for baud rate multilevel modulation communications.

The equalization error is estimated based on the channel ISI levels in a similar manner to conventional Mueller-muller phase detection algorithms. Therefore, the hardware is greatly simplified when compared to previous CTLE adaptation methods. The proposed adaptation is able to calibrate the CTLE source resistance and capacitance simultaneously and independently in contrast to previously published methods. Hence, a wider equalization range can be achieved for a variety of channel loss configurations. The distinct main building blocks in the receiver are modeled and the multiple loop interactions with the CTLEs are analyzed and verified. The proposed adaptation performance is also verified for a wide range of channel losses in two base configurations. The achieved equalization results are close to the optimum solution while being able to provide stable performance over environment variations with a background operation. Future work could address adaptation methods to target the minimum ISI, other CTLE topologies and control schemes.

REFERENCES
[1] Y. Segal, A. Laufer, A. Khairi, Y. Krupnik, M. Cusmai, I. Levin, A. Gordon, Y. Sabag, V. Rahinski, G. Ori, N. Familia, S. Litski, T. Warshavsky, U. Virobnik, Y. Horwitz, A. Balankutty, S. Kiran, S. Palermo, P. M. Li, and A. Cohen, "A 1.41pJ/b 224Gb/s PAM-4 SerDes receiver with 31dB loss compensation," in *IEEE Int. Solid-State Circuits Conf. (ISSCC) Dig. Tech. Papers*, vol. 65, Feb. 2022, pp. 114–116.

[2] J. Kim, S. Kundu, A. Balankutty, M. Beach, B. C. Kim, S. T. Kim, Y. Liu, S. K. Murthy, P. Wali, K. Yu, H. S. Kim, C.-C. Liu, D. Shin, A. Cohen, Y. Segal, Y. Fan, P. Li, and F. O'Mahony, "A 224-Gb/s DAC-based PAM-4 quarter-rate transmitter with 8-tap FFE in 10-nm FinFET," *IEEE J. Solid-State Circuits*, vol. 57, no. 1, pp. 6–20, Jan. 2022.

[3] Y. Frans, J. Shin, L. Zhou, P. Upadhyaya, J. Im, V. Kireev, M. Elzeftawi, H. Hedayati, T. Pham, S. Asuncion, C. Borrelli, G. Zhang, H. Zhang, and K. Chang, "A 56-Gb/s PAM4 wireline transceiver using a 32-way time-interleaved SAR ADC in 16-nm FinFET," *IEEE J. Solid-State Circuits*, vol. 52, no. 4, pp. 1101–1110, Apr. 2017.

[4] (2023). *A Look Into Channels for High Connectivity and Scalable Systems and Initial Considerations for COM*. [Online]. Available: https://www.ieee802.org/3/ck/public/18_11/kareti_3ck_01a_1118.pdf

[5] Z. Guo, A. Elshazly, B. Chen, B. Wang, and A. Mostafa, "A 112.5Gb/s ADC-DSP-based PAM-4 long-reach transceiver with >50dB channel loss in 5 nm FinFET," in *IEEE Int. Solid-State Circuits Conf. (ISSCC) Dig. Tech. Papers*, vol. 65, Feb. 2022, pp. 116–118.

[6] H. Lin, C. Boecker, M. Hossain, S. Tangirala, R. Vu, S. D. Vamvakos, E. Groen, S. Li, P. Choudhary, N. Wang, M. Shibata, H. Taghavi, M. van Ierssel, A. Maniyar, A. Wodkowski, K. Brar, N. Nguyen, and S. Desai, "ADC-DSP-based 10-to-112-Gb/s multi-standard receiver in 7-nm FinFET," *IEEE J. Solid-State Circuits*, vol. 56, no. 4, pp. 1265–1277, Apr. 2021.

[7] H. Park, "A 4.63pJ/b 112Gb/s DSP-based PAM-4 transceiver for a large-scale switch in 5nm FinFET," in *Proc. IEEE Int. Solid- State Circuits Conf. (ISSCC)*, Feb. 2023, pp. 5–7.

[8] B. Zhang, A. Vasani, A. Sinha, A. Nilchi, H. Tong, L. Rao, K. Khanoyan, H. Hatamkhani, X. Yang, X. Meng, A. Wong, J. Kim, P. Jing, Y. Sun, A. Nazemi, D. Liu, A. Brewster, J. Cao, and A. Momtaz, "6.1 A 112Gb/s serial link transceiver with 3-tap FFE and 18-tap DFE receiver for up to 43dB insertion loss channel in 7 nm FinFET technology," in *IEEE Int. Solid-State Circuits Conf. (ISSCC) Dig. Tech. Papers*, Feb. 2023, pp. 5–7.

[9] (2023). *IEEE 802.3ck 100 Gb/s, 200 Gb/s, 400 Gb/s Electrical Interfaces Task Force*. [Online]. Available: https://www.ieee802.org/3/ck/public/tools/

[10] J. Lee, "A 20-Gb/s adaptive equalizer in 0.13-μm CMOS technology," *IEEE J. Solid-State Circuits*, vol. 41, no. 9, pp. 2058–2066, Sep. 2006.

[11] F. Gerfers, G. W. den Besten, P. V. Petkov, J. E. Conder, and A. J. Koellmann, "A 0.2–2 Gb/s 6x OSR receiver using a digitally self-adaptive equalizer," *IEEE J. Solid-State Circuits*, vol. 43, no. 6, pp. 1436–1448, Jun. 2008.

[12] J. Lee, K. Lee, H. Kim, B. Kim, K. Park, and D.-K. Jeong, "A 0.1-pJ/b/dB 1.62-to-10.8-Gb/s video interface receiver with jointly adaptive CTLE and DFE using biased data-level reference," *IEEE J. Solid-State Circuits*, vol. 55, no. 8, pp. 2186–2195, Aug. 2020.

[13] B. Dehlaghi, S. Shahramian, J. Liang, R. Bespalko, D. Dunwell, J. Bailey, B. Wang, A. Sharif-Bakhtiar, M. O'Farrell, K. Tang, A. Chan Carusone, D. Cassan, and D. Tonietto, "A 1.41-pJ/b 56-Gb/s PAM-4 receiver using enhanced transition utilization CDR and genetic adaptation algorithms in 7-nm CMOS," *IEEE Solid-State Circuits Lett.*, vol. 2, no. 11, pp. 248–251, Nov. 2019.

[14] J. Im, "A 112-Gb/s PAM-4 long-reach wireline transceiver using a 36-way time-interleaved SAR ADC and inverter-based RX analog front-end in 7-nm FinFET," *IEEE J. Solid-State Circuits*, vol. 56, no. 1, pp. 7–18, Jan. 2021.

[15] P. W. de Abreu Farias Neto, K. Hearne, I. Chlis, D. Carey, R. Casey, B. Griffin, F. S. F. Ngankem Ngankem, J. Hudner, K. Geary, M. Erett, A. Laraba, H. Eachempatti, J. W. Kim, H. Zhang, S. Asuncion, and Y. Frans, "A 112–134-Gb/s PAM4 receiver using a 36-way dual-comparator TI-SAR ADC in 7-nm FinFET," *IEEE Solid-State Circuits Lett.*, vol. 3, pp. 138–141, 2020.

[16] B.-J. Yoo, "6.4 A 56Gb/s 7.7 mW/Gb/s PAM-4 wireline transceiver in 10 nm FinFET using MM-CDR-based ADC timing skew control and low-power DSP with approximate multiplier," in *IEEE Int. Solid-State Circuits Conf. (ISSCC) Dig. Tech. Papers*, 2020, pp. 122–124.

[17] K. Sun, G. Wang, Q. Zhang, S. Elahmadi, and P. Gui, "A 56-GS/s 8-bit time-interleaved ADC with ENOB and BW enhancement techniques in 28-nm CMOS," *IEEE J. Solid-State Circuits*, vol. 54, no. 3, pp. 821–833, Mar. 2019.

[18] K. Tyagi and B. Razavi, "Performance bounds of ADC-based receivers due to clock jitter," *IEEE Trans. Circuits Syst. II, Exp. Briefs*, vol. 70, no. 5, pp. 1749–1753, May 2023.

[19] B. Razavi, "Jitter-power trade-offs in PLLs," *IEEE Trans. Circuits Syst. I, Reg. Papers*, vol. 68, no. 4, pp. 1381–1387, Apr. 2021.

[20] K. Yadav, P.-H. Hsieh, and A. C. Carusone, "Loop dynamics analysis of PAM-4 Mueller–Müller clock and data recovery system," *IEEE Open J. Circuits Syst.*, vol. 3, pp. 216–227, 2022.

[21] H. Uchiki, Y. Ota, M. Tani, Y. Hayakawa, and K. Asahina, "A 6Gb/s RX equalizer adapted using direct measurement of the equalizer output amplitude," in *Proc. IEEE Int. Solid-State Circuits Conf. Dig. Tech. Papers*, Feb. 2008, pp. 104–599.

[22] K. Mueller and M. Müller, "Timing recovery in digital synchronous data receivers," *IEEE Trans. Commun.*, vol. COM-24, no. 5, pp. 516–531, May 1976.

[23] V. Stojanovic, A. Ho, B. W. Garlepp, F. Chen, J. Wei, G. Tsang, E. Alon, R. T. Kollipara, C. W. Werner, J. L. Zerbe, and M. A. Horowitz, "Autonomous dual-mode (PAM2/4) serial link transceiver with adaptive equalization and data recovery," *IEEE J. Solid-State Circuits*, vol. 40, no. 4, pp. 1012–1026, Apr. 2005.

[24] J. G. Proakis, *Digital Communications*. New York, NY, USA: McGraw-Hill, 2008.

[25] B. Saltzberg, "Intersymbol interference error bounds with application to ideal bandlimited signaling," *IEEE Trans. Inf. Theory*, vol. IT-14, no. 4, pp. 563–568, Jul. 1968.

[26] J. W. M. Bergmans, "Effect of binary modulation codes with rate R=1/N on equivalent discrete-time models for channels with intersymbol interference," *IEEE Trans. Inf. Theory*, vol. 38, no. 5, pp. 1587–1592, Jun. 1992.

[27] J. Cao, "21.7 A 500mW digitally calibrated AFE in 65 nm CMOS for 10Gb/s serial links over backplane and multimode fiber," in *IEEE Int. Solid-State Circuits Conf. (ISSCC) Dig. Tech. Papers*, Oct. 2009, pp. 370–371.

[28] K. Gopalakrishnan, "3.4 a 40/50/100Gb/s PAM-4 Ethernet transceiver in 28 nm CMOS," in *IEEE Int. Solid-State Circuits Conf. (ISSCC) Dig. Tech. Papers*, Jan. 2016, pp. 62–63.

[29] S. Kiran, S. Cai, Y. Luo, S. Hoyos, and S. Palermo, "A 52-Gb/s ADC-based PAM-4 receiver with comparator-assisted 2-bit/Stage SAR ADC and partially unrolled DFE in 65-nm CMOS," *IEEE J. Solid-State Circuits*, vol. 54, no. 3, pp. 659–671, Mar. 2019.

[30] B. Zand, M. Bichan, A. Mahmoodi, M. Shashaani, J. Wang, R. Shulyzki, J. Guthrie, K. Tyshchenko, J. Zhao, E. Liu, N. Soltani, A. Freeman, R. Anand, S. Rubab, R. Khela, S. Sharifian, and K. Herterich, "A 1-58.125Gb/s, 5-33dB IL multi-protocol Ethernet-compliant analog PAM-4 receiver with 16 DFE taps in 10nm," in *Proc. IEEE Int. Solid-State Circuits Conf. (ISSCC)*, vol. 65, Feb. 2022, pp. 1–3.

[31] (2023). *A Collection of Cabled Backplane Prototype Channels for 200Gb/s Per Lane For.3df PHY Type Development*. [Online]. Available: https://www.ieee802.org/3/df/public/adhoc/electrical/22_0502/mellitz_3df_elec_01_220502.pdf

[32] D. M. Pozar, *Microwave Engineering*. Hoboken, NJ, USA: Wiley, 2011.

[33] S. Bottacchi, *Noise and Signal Interference in Optical Fiber Transmission Systems: an Optimum Design Approach*. Hoboken, NJ, USA: Wiley, 2008.

[34] Y. A. Tavares, S. Kim, and M. Lee, "A background M-channel time-interleaved ADC calibration for multilevel modulations based on the probability density function difference and a greedy algorithm," *IEEE Trans. Signal Process.*, vol. 70, pp. 4140–4155, 2022.

[35] D. E. Seborg, T. F. Edgar, D. A. Mellichamp, and F. J. Doyle III, *Process Dynamics and Control*. Hoboken, NJ, USA: Wiley, 2016.

[36] E. Bristol, "On a new measure of interaction for multivariable process control," *IEEE Trans. Autom. Control*, vol. AC-11, no. 1, pp. 133–134, Jan. 1966.

[37] J. Bailey, H. Shakiba, E. Nir, G. Marderfeld, P. Krotnev, M.-A. LaCroix, D. Cassan, and D. Tonietto, "A 112-Gb/s PAM-4 low-power nine-tap sliding-block DFE in a 7-nm FinFET wireline receiver," *IEEE J. Solid-State Circuits*, vol. 57, no. 1, pp. 32–43, Jan. 2022.

YANG AZEVEDO TAVARES (Student Member, IEEE) was born in Natal, Brazil, in 1996. He received the B.S. degree (Hons.) in computer engineering from the Federal University of Rio Grande do Norte, Natal, Brazil, in 2019, in collaboration with California State University, East Bay, Hayward, CA, USA. He is currently pursuing the combined M.S. and Ph.D. degrees with the Department of Electrical Engineering and Computer Science, Gwangju Institute of Science and Technology, Gwangju, South Korea. His research interest includes high-speed mixed-signal processing systems and circuits.

MINJAE LEE (Senior Member, IEEE) received the B.Sc. and M.S. degrees in electrical engineering from Seoul National University, Seoul, South Korea, in 1998 and 2000, respectively, and the Ph.D. degree in electrical engineering from the University of California at Los Angeles, Los Angeles, CA, USA, in 2008. In 2000, he was a Consultant with GCT Semiconductor Inc., San Jose, CA, USA, and Silicon Image Inc., Sunnyvale, CA, USA, designing analog circuits for wireless communication and digital signal processing blocks for Gigabit Ethernet. In 2001, he joined Silicon Image Inc., to develop Serial ATA products. In August 2008, he joined Agilent Technologies, Santa Clara, CA, USA, where he was involved with the development of next-generation high-speed ADCs and DACs. Since 2012, he has been with the School of Electrical Engineering and Computer Science, Gwangju Institute of Science and Technology, Gwangju, South Korea, where he is currently a Professor. He was a recipient of the 2007 Best Student Paper Award from the VLSI Circuits Symposium, Kyoto, Japan, and the GIST Distinguished Lecture Award, in 2015.

• • •